Supplementary Materials for

Nanophotonic rare-earth quantum memory with optically controlled retrieval

Tian Zhong, Jonathan M. Kindem, John G. Bartholomew, Jake Rochman, Ioana Craiciu, Evan Miyazono, Marco Bettinelli, Enrico Cavalli, Varun Verma, Sae Woo Nam, Francesco Marsili, Matthew D. Shaw, Andrew D. Beyer, Andrei Faraon*

*Corresponding author. Email: faraon@caltech.edu

Published 31 August 2017 on *Science* First Release
DOI: 10.1126/science.aan5959

This PDF file includes:

1 Materials and Methods

Nd:YVO nanocavity design and fabrication The triangular nanobeam has a width of 690 nm. 31 (11 on one side of the cavity defect mode and 20 on the other side) periodic subwavelength grooves with widths of 147 nm along the beam axis were milled on top of the nanobeam. The period of the grooves was modulated quadratically over 14 grooves to form defect modes in

the photonic bandgap (*16*). The fundamental TM mode, with top side views shown in Fig. 1C, is chosen because it aligns with the strongest Nd dipole of the 879.7 nm transition along c axis of YVO crystals. The theoretical quality factor is 1×10^5 for the asymmetric cavity, and 2×10^6 for the symmetric cavity (20 grooves on both sides). The left-most groove interfacing the waveguide was tapered to minimize scattering. The scattering due to this taper was negligibly small from optical microscope measurements. The efficiency of the coupler was determined to be 27% by comparing the cavity-reflected power at a off resonance wavelength (in the photonic bandgap) to that from a flat surface of known reflectivity.

The optimization procedure for a one-sided cavity was started by fabricating symmetric two-sided nanocavities with sufficiently long mirrors (20 grooves) on each side of the cavity mode. The measured Q was in the range of 20,000 to 40,000, corresponding to an intrinsic loss (likely due to surface scattering) rate $\kappa_{\rm sc}$=$2\pi\times$9-18 GHz. In subsequent devices, the number of grooves on one side was decremented from 20 to 11, and the corresponding Q decreased from 20,000 to 3,700 (κ= $2\pi\times$90 GHz). The final device (with 11 grooves on the input side) was expected to be dominantly one-sided and over-critically coupled with the waveguide: $\kappa_{\rm in}/\kappa$=0.8. In reality, the measured reflection spectrum in Fig. 2A shows a near critical coupling to the waveguide with $\kappa_{\rm in}$ $\sim$0.5κ=$2\pi\times$45 GHz. The deviation from the design might be due to additional fabrication imperfections when making highly asymmetric groove patterns, which could be improved in future fabrication processes.

Preparation and probing of an atomic frequency comb in the nanocavity The comb in Fig. 3D was prepared with 1500 pairs of pulses each containing $\sim$100 photons (at the input to the cavity). The comb was read out as modulated cavity reflection spectrum using a weak probe field. The profile of the comb in terms of atomic spectral density was normalized to an empty cavity (i.e. 0 ions), and to the full population when no preparation was performed (i.e. 100% ion density). To convert the reflection spectrum to a normalized atomic density, we used the ex-

pression $R(\omega) = 1 - T_0(1 + 4N(\omega)g^2/\kappa\Gamma_h)^{-2}$, where $T_0 = 0.9$ takes into account the residual on-resonance reflection of a bare cavity (i.e. N=0). This expression assumes negligible correlation between ions of different frequencies, which is valid for an inhomogeneous ensemble that is coupled to a cavity below the strong collective coupling regime (*15*).

Efficiency of AFC optical quantum memory based on a nanophotonic cavity Taking into account the cavity QED effects (e.g. Purcell enhancement) present in a nanocavity, we derive the following device storage efficiency from the Tavis-Cummings Hamiltonian method as in (*21*).

$$\eta_{\mathrm{dev}} = \left(\frac{4\kappa_{\mathrm{in}}\Gamma_{\mathrm{comb}}}{(\kappa + \Gamma_{\mathrm{comb}} + \Gamma_{\mathrm{bg}})^2} \right)^2 e^{-7/F^2} \tag{1}$$

The storage process - mapping of a input photon onto a dipole excitation in the cavity - has an efficiency of $4\kappa_{\mathrm{in}}\Gamma_{\mathrm{comb}}/(\kappa + \Gamma_{\mathrm{comb}} + \Gamma_{\mathrm{bg}})^2$ where $\Gamma_{\mathrm{comb}} = n_{\mathrm{comb}}g^2/\gamma_h$, $\Gamma_{\mathrm{bg}} = n_{\mathrm{bg}}g^2/\gamma_h$ are Purcell-enhanced atomic absorption rates per bandwidth for ions contributing to the comb and the background, respectively (n_{comb} and n_{bg} are atomic number densities for the comb and the background). The retrieval process - emission of AFC photon echo to the waveguide - is an exact time-reversal of the storage process, therefore having the same efficiency. The additional dephasing due to the comb is given by the term e^{-7/F^2} assuming Gaussian-shaped teeth (*13*). The conditions to approach unity efficiency are $\kappa_{\mathrm{in}}/\kappa \sim 1$, $\Gamma_{\mathrm{bg}} = 0$, $F \gg 1$, and $\Gamma_{\mathrm{comb}} = \kappa$. The last condition is the perfect cavity-ensemble impedance-matching condition that could almost be met with the current nanocavity devices.

Measurement of time-bin qubit fidelity We used attenuated laser pulses to generate test time-bin qubit states $|e\rangle$, $|l\rangle$, $|+\rangle$, $|-\rangle$. The fidelity $F_{e(l)}$ for input state $|e(l)\rangle$ is determined experimentally as $F_{e(l)} = C_{e(l)}/(C_{e(l)} + C_{l(e)})$ where $C_{e(l)}$ is the number of counts in the early (late) time bin. For states $|+\rangle$, the recalled photons were sent through a qubit analyzer consisting of a fibre-based unbalanced Mach-Zehnder interferometer with a long-short path difference δ_t=30 ns that was matched with the time separation between early and late bins. The interferometer was

phase-stabilized, and the phase difference between long-short paths (0 or π) was set by a piezo-electric fibre stretcher. The fidelity is determined by $F_{+(-)} = C_{+(-)}/(C_{+(-)} + C_{-(+)})$ where $C_{+(-)}$ is the counts at the interferometer output when the phase is set to 0(π). The fidelity parameters $F_{e,l,+,-}$ were measured at two different mean photon numbers α_1=0.26, α_2=0.58, from which the lower bounds on the single-photon qubit fidelity $F^{(1)}_{e,l,+,-}$ were calculated (Supplementary section 7). The average qubit fidelity is then $F = \frac{1}{3}F^{(1)}_{e/l} + \frac{2}{3}F^{(1)}_{+/-}$.

AC Stark pulse generation and spectral compression of AFC The AC Stark pulses detuned at $\pm$1 GHz from the center of the AFC were generated by driving the phase electro-optic modulator (EOM) at a 2.4 V_π voltage for a duration of 16 ns. The first-order sidebands constituted the Stark pulses, and the extinction of the zero-order power was about -20 dB. The second and higher order sidebands also contribute to AC Stark shifts of AFC, but their effects dropped off quadratically. The photon numbers in Fig. 4C-E represent only the number in the first-order sidebands. We estimate the single photon Stark Rabi frequency to be $\sim 2\pi\times$30 MHz (*22*) in the nanocavity. The theoretical compression of the AFC comb spacing $\delta\Delta$ is 48 kHz per Stark photon in the cavity.

2 Additional details of the experiment apparatus

Single photon detectors The WSi superconducting nanowire single photon detector (SNSPD) has a system detection efficiency of 82$\pm$2.4% at 880 nm measured at 480 mK. The detector dark count rate is $<$10 counts per second at a bias current of 5.0 μA with the critical current at 6.3 μA.

Optical pulse generation and shuttering The optical pulses were generated by first passing the CW laser output (M Squared Solstis) through two AOMs (Isomet 1250c), both in double-pass configuration, in series, which produced a minimum pulse width of 50 ns with a 120 dB extinction ratio. Then the pulses were further trimmed down to a minimum of 8 ns using an

intensity EOM (Jenoptik) with an extinction ratio of 30 dB. For fidelity measurements on $|+/-\rangle$ qubit states, an additional phase EOM was used in the fibre path to generate a 0 or π phase shift between the two time bins. During the optical pumping sequence, the optical MEMS switch was off (extinction of 60 dB) to avoid blinding and latching of the SNSPD.

System transmission efficiency The system transmission efficiency including the waveguide to fiber coupling (27%), the fiber splicing and connectors loss (50% transmission in total), circulator loss (49.2% transmission), optical MEMS switch loss (72.5% transmission), and detector efficiency is 3.95%.

3 Modelling optical pumping dynamics in Nd:YVO

We consider a Λ-system with ρ_1, ρ_2 and ρ_3 being the population fraction in the two ground states and in the excited state, respectively. We also introduce an effective fourth level ρ_4 that takes into account decays from the excited state to other crystal field levels (Z_{2-5}, e.g.1064 nm transition of Nd:YVO), and then relaxes quickly to either of the Zeeman ground states. Optically pumping populations between ground state spin levels (through excitation and incoherent relaxation) can be modelled with a set of rate equations.

$$\frac{d}{dt}\rho_1 = w_{21}\rho_2 - w_{12}\rho_1 + \Omega_{31}\rho_3 - \Omega_{13}\rho_1 + w_{41}\rho_4 \quad (2)$$

$$\frac{d}{dt}\rho_2 = w_{12}\rho_1 - w_{21}\rho_2 + A_{32}\rho_3 + w_{42}\rho_4 \quad (3)$$

$$\frac{d}{dt}\rho_3 = \Omega_{13}\rho_1 - \Omega_{31}\rho_3 - A_{32}\rho_3 - A_{34}\rho_3 \quad (4)$$

$$\frac{d}{dt}\rho_4 = A_{34}\rho_3 - w_{41}\rho_4 - w_{42}\rho_4. \quad (5)$$

where w_{ij} are the spin relaxation rates between the ground states i, j. w_{41}, w_{42} represent the spin decay from higher-lying crystal-field levels, that are very fast (on the order of ps). A_{3j} are the spontaneous emission rates between excited state 3 and ground state j. $\Omega_{31}, \Omega_{13} \gg A$ is the

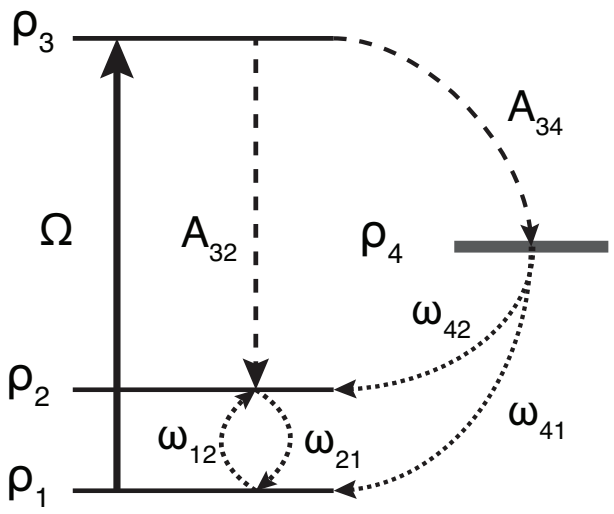

Figure S1: **Energy level scheme of Nd:YVO for modelling the optical pumping dynamics.**

Rabi frequency assuming an intense optical pumping laser on resonance with the transition 1-3 is driving the transition with equal absorption and emission rates. In the steady state, $d\rho/dt = 0$ and $\rho_1 = \rho_3$. Then the spin polarization, that is the ratio of populations between the two ground states, is given by

$$\frac{\rho_2}{\rho_1} = \frac{w_{12} + A_{32} + A_{34}w_{42}/(w_{42} + w_{41})}{w_{21}} \approx 1 + \frac{2T_z(\beta_{32} + \beta_{34}w_{42}/(w_{42} + w_{41}))}{T_1} \qquad (6)$$

where the second approximation assumes $w_{12} = w_{21} = 1/2T_z$ which is valid when the thermal energy k_BT is larger than the Zeeman splitting. The relevant branching ratios β_{32}, β_{34} are the probability that ions in the excited state decay to the Zeeman state 2 or the lumped effective crystal field level 4. To achieve efficient optical pumping and strong spin polarization, it is therefore desirable to have a Zeeman lifetime T_Z that is considerably longer than the relevant spontaneous decay time $1/A_{32} = T_1/\beta_{32}$ or $1/A_{34}$. In general, the condition $T_z \gg T_1$ does not hold for Kramers ions even at temperatures below 4 K. This factor, combined with poor branching ratios, generally results in inefficient holeburning for Kramer ions including erbium and neodynium. Here our strategy is to increase A_{32} via Purcell enhancement using an optical

nanocavity, creating a situation in which optical pumping can be enhanced.

The spontaneous decay rate of a transition coupled to an optical cavity is enhanced by the Purcell factor $F + 1$, where F is

$$F = \frac{3}{4\pi^2}\left(\frac{\lambda}{n}\right)^3\left(\frac{Q}{V}\right)\int_V\left(\frac{E(\mathrm{r})\cdot\mu}{|E_{\max}||\mu|}\right)^2, \tag{7}$$

where the last integral over the mode volume of the cavity takes into account the local field intensities experienced by the atoms which are randomly distributed in the cavity. The spontaneous decay rate γ from the optical excited state will be modified according to

$$\gamma = \frac{(F_{31}+1)\beta_{31}}{T_1} + \frac{(F_{32}+1)\beta_{32}}{T_1} + \gamma_{\mathrm{indirect}} \tag{8}$$

where both 1-3, 2-3 transitions are assumed to be coupled to the cavity with the same Purcell factor because their splitting is much less than the cavity linewidth, whereas $\gamma_{\mathrm{indirect}}$ takes into account decay to other crystal-field levels that are not coupled to the cavity (i.e. other four Kramers doublets Z_2-Z_5, which include the 1064 nm transition). The Purcell enhancement effect shortens the total excited state lifetime, and also effectively increases the branching ratios of transitions coupled to the cavity.

For clarity, here we focus on the steady state ρ_1 that can be calculated from Eq. (4), given $\rho_2 + \rho_1 = 1$. To model the experimental conditions, a few additional factors need to be taken into account:

1. The branching ratio $\beta_{32}(\theta)$ is determined from the spin Hamiltonian for any given magnetic field orientation θ with respect to c-axis, as well as the fact $\beta_{32}+\beta_{31} = T_1/T_{\mathrm{spon}}$=0.273 in a bulk crystal calculated from the spontaneous decay time T_{spon} to the $^4I_{9/2}$ level.

2. The percentage of ions belonging to the odd nuclear spin isotope, which has a different spin Hamiltonian.

3. The finite spin population relaxation between turning off the optical pumping laser and the time when the spin population is read out.

The second factor in the list above can be included by separating the ensemble of ions into subgroups. Odd-isotope ions will in general hole burn very well because the hyperfine ground states are mixed and they have long nuclear spin lifetimes (>100 ms) for trapping the population (*33*). The expression to include these physical situations is

$$\rho_1(0) = \alpha_{\rm E}\frac{1/2}{1+\frac{T_z((F_{32}+1)\beta_{32}^{(\rm E)}+\beta_{34}\beta_{\rm ID}^{(\rm E)})}{T_1}} + \alpha_{\rm O}\frac{1/2}{1+\frac{T_{HF}((F_{32}+1)\beta_{32}^{(\rm O)}+\beta_{34}\beta_{\rm ID}^{(\rm O)})}{T_1}} \tag{9}$$

$$\tag{10}$$

where $\alpha_{\rm E}$ and $\alpha_{\rm O}$ ($\alpha_{\rm E}+\alpha_{\rm O}=1$) represent the percentages of even and odd isotopes. We know that $\alpha_{\rm E} =^{(142)} 0.272 +^{(144)} 0.238 +^{(146)} 0.172 +^{(148)} 0.057 +^{(150)} 0.056 = 0.795$, and $\alpha_{\rm O} = 0.205$. The term $\beta_{\rm ID} = w_{42}/(w_{42}+w_{41}))$ is introduced to track the effective branching ratio for spin relaxation via the indirect path. The precise value of this term is unknown, but we characterize it with the same Nd:YVO crystal sample at 3.5 K (results in the next section). Generally, excited ions decaying to the ground states via intermediate levels tend to hole burn well because spin flips are induced during the time spent in intermediate states. Furthermore, the hyperfine states in Nd:YVO have considerably longer lifetime, i.e. T_{HF} =320 ms, that effectively traps the population away from the ground state 1. Consequently the values for $\beta_{32}^{(O)}$ and $\beta_{\rm ID}^{(O)}$ are not critical as the odd isotopes holeburn very efficiently and contribute almost none to the ground state population ρ_1 during the time scale of consideration ($\leq$50 ms). Lastly, we have $\beta_{34} = 1-\beta_{31}-\beta_{32}$=0.727. To include the third factor in the list above, the population in ρ_1 after a time τ after the end of the optical pumping pulse is

$$\rho_1(\tau) = \rho_1(0) + (\rho_1(\infty)-\rho_1(0))\exp^{-\tau/T_Z} \quad , \tag{11}$$

where $\rho_1(\tau)$ is the population at time τ after the optical pumping laser is off.

Below we discuss the parameters relevant for optical pumping dynamics in two cases. **Case 1: In the photonic nanocavity**

- The ensemble averaged Purcell factor is $F_{31} = F_{32} \approx 70$, derived considering the shortening of T_1 from 90 μs to 4.5μs shown in Fig. 2B in the main text.

- $\beta_{32}(\theta)$ is given by the spin Hamiltonians of the $^4I_{9/2}$ and $^4F_{3/2}$ levels, and the magnetic field angle relative to the c-axis (θ) (*24*)

- $T_Z(\theta)$ is the Zeeman lifetime, which is also a function of magnetic field angle θ. With a field of 350 mT oriented approximately along the c-axis, the lifetime at 480 mK is approximately 12.5 ms. Currently, our measurements at 480 mK does not allow changing field angles away from c axis. However, prior results indicate that the electron spin lifetime at a 350 mT field is limited by resonant spin-spin interactions (*10*).

- wait time τ =200 μs, which is $\sim$40 times the cavity T_1.

Case 2: In the bulk crystal

- $F_{32} = 1$ in the absence of Purcell enhancement

- $\beta_{\mathrm{SH}}(\theta)$ is given by the spin Hamiltonians of the $^4I_{9/2}$ and $^4F_{3/2}$ levels and the magnetic field angle relative to the c-axis (θ) (*24*)

- $T_Z(\theta)$ is the bulk Zeeman lifetime as a function of magnetic field angle θ, which is expected to be limited by the spin-spin interactions as in the previous case.

- wait time τ =2 ms, which is $\sim$20 times the bulk T_1.

4 Extracting Nd:YVO optical pumping properties

The simple model described in the previous section allows the optical pumping dynamics to be predicated from Eq. (8) with the knowledge of T_z, F_{32}, β_{32} and β_{ID} for a given experimental condition. Among these parameters, T_z, F_{32}, β_{32} can be directly measured in experiments. β_{ID} cannot be measured but is possible to infer its value from the remaining ground state population $\rho_1(\tau)$ after optical pumping. We assume β_{ID} has a dominant functional dependence on the field angle, and is not sensitive to temperatures (in the range below 4 K) and field strengths (below 1 T).

We performed a set of optical pumping experiments in a 0.5 mm-think Nd:YVO bulk sample that is cut from the same boule (nominally 100 p.p.m.) as the one on which nanocavities were fabricated. The results are summarized in Fig. S2. The sample was mounted in a cryostation (Montana Instruments) at 3.6 K. The magnetic field generated from a pair of rare-earth permanent magnets was 340 mT, and its orientation θ with respect to the crystal c-axis was varied manually. The branching ratio β_{32} in Fig. S2 was extracted from the absorption spectra of the transitions 1-3 and 1-2, which agree with the theoretical Spin Hamiltonian calculations (*24*) (blue curve). The optical pumping laser was polarized along the c axis, and was on for a sufficiently long time such that a maximal spin polarization was achieved. Then the spectral hole (measured as an increase in transmission) was probed by a weak pulse at increasing delays from the optical pumping pulse. From the decay of the spectral hole depth, we extracted the Zeeman lifetime T_z at each field orientation. Then based on the remaining ground state population, we estimate the effective β_{ID} values from Eq. (8). There was a clear trend of increasing β_{ID} (increasing spin mixing via other crystal field levels) with θ. For the experimental configuration described in the main text, the field angle is nearly along the c-axis, thus we expect $\beta_{32}, \beta_{\mathrm{ID}} \to 0$. This means the optical pumping efficiency is expected to be low (poor spin po-

larization) in the absence of cavity enhancement. In the meantime, the enhancement of optical pumping by the Purcell effect is expected to be most pronounced in such a field configuration.

5 Estimation of the magnetic field orientation

In Fig. S3, we show measurements of the absorption spectrum of the 0.5 mm thick bulk Nd:YVO crystal in which the device was fabricated. The bulk crystal experienced the same field as the ions in the cavity assuming negligible field inhomogeneity across the sample thickness. The probe light was polarized perpendicular to c axis, which caused the branching ratios of four Zeeman split transitions to be different from the configuration with the probe polarized along c-axis (*24*). The transitions a, c are overlapped, whereas the transitions b, d are clearly resolved and they are split by 9.92 GHz.

Each ground and excited doublet Z_1 and Y_1 is characterized by the principal values $g_\perp$ (perpendicular to c) and $g_\parallel$ (parallel to c) of the g-factor. We used the following values for Z_1: $|g_\perp|$= 2.361, $|g_\parallel|$= 0.915; for Y_1: $|g_\perp|$= 0.28, $|g_\parallel|$=1.13. The relative frequencies of the transitions a-d can be then calculated from the effective g-factors at a field angle θ with respect to the c aixs. We measured the field strength at the sample to be 340$\pm$2 mT (from a 1" diameter rod N52 grade rare-earth permanent magnet). In Fig.S3, we plot the expected transition frequencies (black curves) for B=340 mT and varying angles θ. The measured frequency separation between the transition b and d corresponded to a θ=8.2$\pm$1.5°. The red dotted lines are expected transition frequencies for θ=8.2°.

6 Noise performance of the nanophotonic AFC quantum interface

One of the key metrics for an AFC quantum interface is the noise level due to incoherent spontaneous emissions from the ensemble in the time window an echo photon is retrieved. Low-noise

and thus high fidelity memory is typically achieved in bulk rare-earth doped crystals by imposing a long wait time (e.g. 20-40 optical T_1 times) between the input photons and the last pulses in the optical pumping (AFC preparation) sequence. This is to ensure no atoms are in the excited state and the spontaneous emission is absent. In a nanocavity, the optical T_1 is substantially reduced (e.g. $\sim$20 times in Fig. 2B) due to the Purcell effect. Therefore the necessary wait time required to achieve low-noise performance is also reduced. In our AFC experiment in the nanocavity, the wait time was 200 μs, $\sim$40 times the Purcell enhanced T_1^{cav} but only $\sim$2 times the bulk T_1. A typical single-pulse input (mean photon number 0.58) and the echo signal after a storage time of 75 ns is plotted in Fig. S4A. Without subtraction of detector dark counts, the noise level per bin (8 ns) is 17 dB below the peak counts in the echo pulse. This noise level did not decrease when the wait time was increased, for instance, to 2 ms, which indicated that the current noise was not caused by the spontaneous emission from the optical pumping pulses. The remaining noise is likely to be mostly contributed by the background ions (imperfect optical pumping as evidenced in Fig. 3D) absorbing the input photon and emitting spontaneously. Figure S4B plots the AFC echo efficiency versus the storage time. The red data point corresponds to the condition in which the results shown in Fig. 3D, E of the main text are measured.

7 Qubit storage fidelity from decoy-state analysis

For characterization of the memory storage fidelity, we used attenuated laser pulses to mimic true single photons (i.e. Fock state) as inputs to the memory. Decoy state strategy is a general technique that allows extraction of the qubit error rate, after transmission in the context of quantum key distribution or after storage and retrieval in quantum memories, due to the single photon component of a coherent state signal. Experimentally it requires measuring detection error probabilities at 3 different mean photon numbers of the input coherent states: μ_s for signal

state, a non-zero μ_{d1} for the first decoy state, and μ_{d2}=0 (i.e. vacuum) for the second decoy state. Closely following the treatment in (*35, 25*), here we outline the essential steps to derive the lower bound on the single photon qubit storage fidelities from experimentally measured quantities.

First, we define the error rate as $E_\psi = 1 - F_\psi = C_\psi/(C_\psi + C_{\phi_\perp})$, where F is the fidelity defined in the main text. The error E is thus the probability of detection in a wrong basis that is orthogonal to the input state. The error rate $E^{(1)}$ for the single photon component of the coherent pulses is upper bounded by $E_U^{(1)}$ given by

$$\begin{aligned} E^{(1)} \leq E_U^{(1)} &= \frac{E^{(\mu_{d1})} Q^{(\mu_{d1})} e^{\mu_{d1}} E^{(\mu_{d2})} Q^{(\mu_{d2})} e^{mu_{d2}}}{(\mu_{d1} - \mu_{d2}) Y_L^{(1)}} \\ &= \frac{E^{(\mu_{d1})} Q^{(\mu_{d1})} e^{\mu_{d1}} E^{(0)} Y^{(0)}}{\mu_{d1} Y_L^{(1)}}, \end{aligned} \tag{12}$$

where $Y^{(0)}$ and $Y_L^{(1)}$ are the zero-photon yield and the lower bound for the single photon yield, respectively. μ_{d1}=0.26 and μ_{d2}=0 (vaccum) are the mean photon numbers for the two decoy states used in our experiment, and $E^{(\mu_{d1})}$ and $E^{(\mu_{d2})}$=$E^{(0)}$ are the corresponding error probabilities obtained experimentally. The gain $Q^{(\mu)}$ is the detection probability for an echo photon for each input, which reflects the mean photon in the input states, inefficiency of the memory device, the coupling loss from the device to the fiber, and all the losses in the optical path up to and including the detector. Experimentally, the gain was measured by the total echo photon count rate (per second) over the repetition rate of the input signal.

The lower bound on Y_L^1 the single photon yield for the case of μ_{d2}=0 is given by

$$Y^{(1)} \geq Y_L^{(1)} = \frac{\mu_s}{\mu_s \mu_{d1} - \mu_{d1}^2} \left(Q^{(\mu_{d1})} e^{\mu_{d1}} - \frac{\mu_{d1}^2}{\mu_s^2} Q^{(\mu_s)} e^{\mu_s} - \frac{\mu_s^2 - \mu_{d1}^2}{\mu_s^2} Y^{(0)} \right) \tag{13}$$

where μ_s=0.58 is the mean photon number of the signal state. Once the upper bound on the error probability $E_U^{(1)}$ is obtained from Eq. 11, the lower bound on the qubit fidelity is $F_L^{(1)} = 1 - E_U^{(1)}$, which represents the fidelity we would have obtained if true single photons were used to encode

qubits at the memory input. Table I lists the measured fidelities for retrieved qubits at different input photon numbers, from which the single photon qubit fidelities are calculated.

Input photon number	$F_{\mathrm{e/l}}$	$F_{+/-}$
0.58	93.63$\pm$ 0.64%	94.41$\pm$ 0.58%
0.26	94.91$\pm$ 0.81%	92.58$\pm$ 0.65%
1	98.63$\pm$ 0.33%	95.91$\pm$ 0.41%

Table S1: Fidelities of the retrieved time-bin qubits.

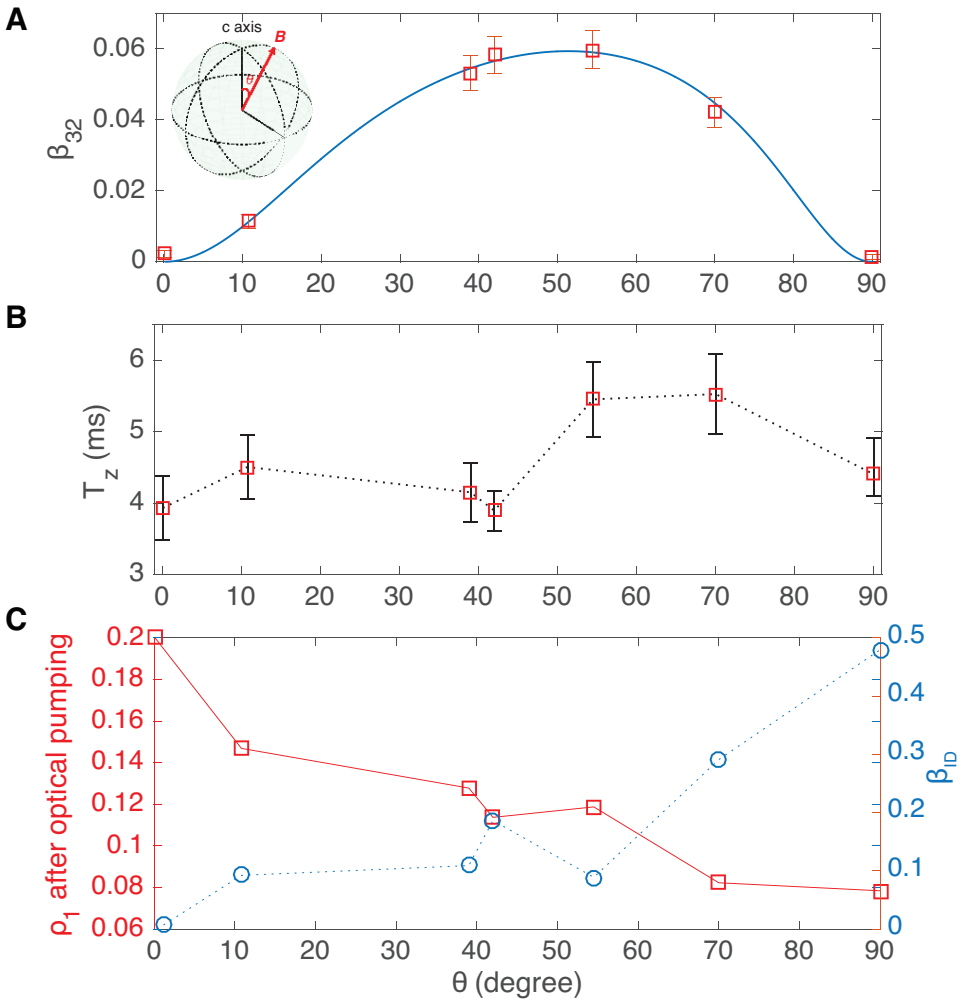

Figure S2: **Characterization of optical pumping properties in a 100 p.p.m. bulk Nd:YVO crystal.** (**A**) β_{32} extracted from absorption spectra of the 1-3, 2-3 transitions. The inset shows the magnetic field angle θ, definited with respect to crystal c axis. (**B**) Measured Zeeman lifetimes T_z as the $1/e$ decay constants of the spectral hole depths. (**C**) Measured remaining ground state population after optical pumping, from which we estimate the effective β_{ID} values at each field angle.

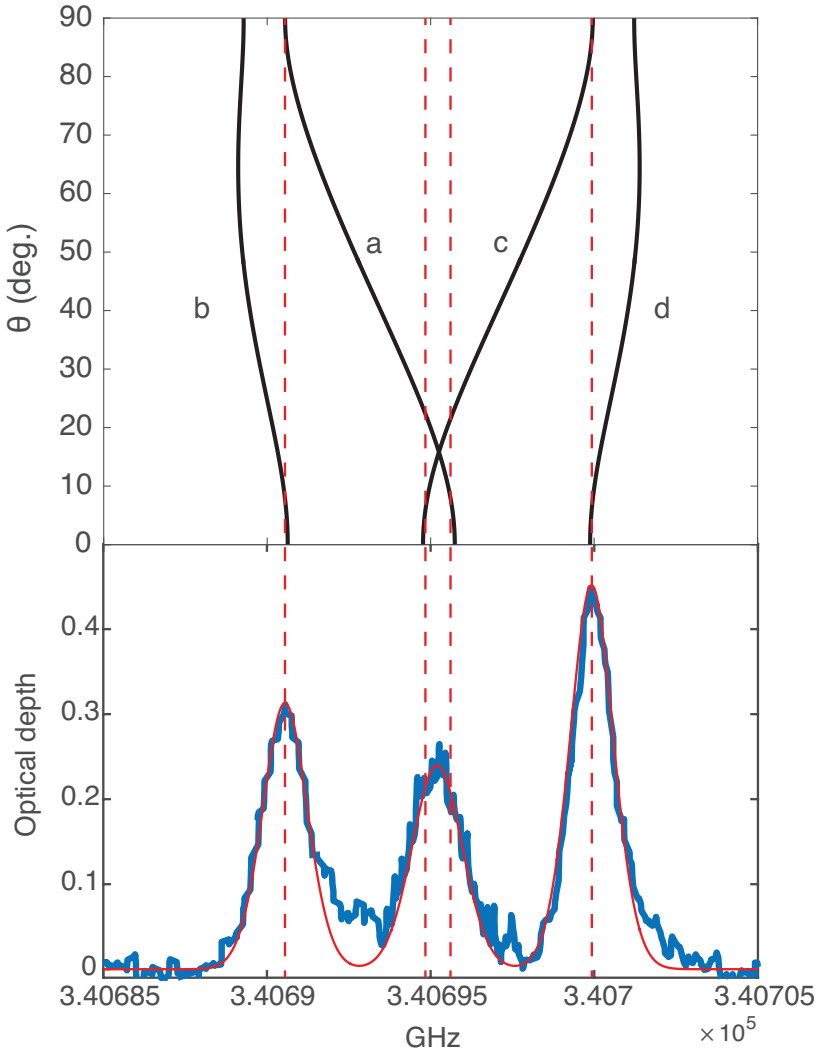

Figure S3: Absorption spectrum of a bulk Nd:YVO at 480 mK (bottom panel) and the expected transition frequencies as a function of magnetic field angle θ with respect to c axis (upper panel). The dotted red lines indicate the expected frequencies of all four optical transitions. From the intersections of the dotted and the black lines, we estimated the magnetic field angle.

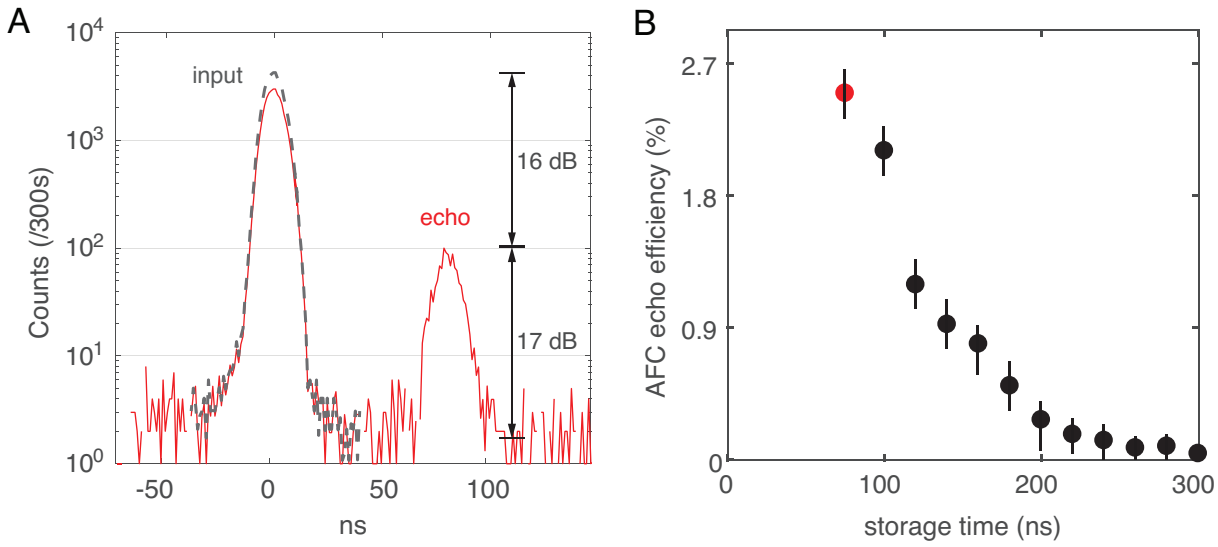

Figure S4: (**A**) A representative single-pulse input and AFC echo photon signal measured in the nanocavity.(**B**) AFC echo efficiency versus storage time. The results shown in Fig. 3D, E of the main text are measured at the condition represented by the red data point.

References and Notes

1. H. J. Kimble, The quantum internet. *Nature* **453**, 1023–1030 (2008). doi:10.1038/nature07127 Medline

2. C. W. Chou, H. de Riedmatten, D. Felinto, S. V. Polyakov, S. J. van Enk, H. J. Kimble, Measurement-induced entanglement for excitation stored in remote atomic ensembles. *Nature* **438**, 828–832 (2005). doi:10.1038/nature04353 Medline

3. H. de Riedmatten, M. Afzelius, M. U. Staudt, C. Simon, N. Gisin, A solid-state light-matter interface at the single-photon level. *Nature* **456**, 773–777 (2008). doi:10.1038/nature07607 Medline

4. A. I. Lvovsky, B. C. Sanders, W. Tittel, Optical quantum memory. *Nat. Photonics* **3**, 706–714 (2009). doi:10.1038/nphoton.2009.231

5. W. Tittel, M. Afzelius, T. Chaneliére, R. L. Cone, S. Kröll, S. A. Moiseev, M. Sellars, Photon-echo quantum memory in solid state systems. *Laser Photonics Rev.* **4**, 244–267 (2010). doi:10.1002/lpor.200810056

6. E. Saglamyurek, N. Sinclair, J. Jin, J. A. Slater, D. Oblak, F. Bussières, M. George, R. Ricken, W. Sohler, W. Tittel, Broadband waveguide quantum memory for entangled photons. *Nature* **469**, 512–515 (2011). doi:10.1038/nature09719 Medline

7. S. Marzban, J. G. Bartholomew, S. Madden, K. Vu, M. J. Sellars, Observation of photon echoes from evanescently coupled rare-earth ions in a planar waveguide. *Phys. Rev. Lett.* **115**, 013601 (2015). doi:10.1103/PhysRevLett.115.013601 Medline

8. G. Corrielli, A. Seri, M. Mazzera, R. Osellame, H. de Riedmatten, Integrated optical memory based on laser-written waveguides. *Phys. Rev. Appl.* **5**, 054013 (2016). doi:10.1103/PhysRevApplied.5.054013

9. C. W. Thiel, T. Böttger, R. L. Cone, Rare-earth-doped materials for applications in quantum information storage and signal processing. *J. Lumin.* **131**, 353–361 (2011). doi:10.1016/j.jlumin.2010.12.015

10. Y. Sun, C. W. Thiel, R. L. Cone, R. W. Equall, R. L. Hutcheson, Recent progress in developing new rare earth materials for hole burning and coherent transient applications. *J. Lumin.* **98**, 281–287 (2002). doi:10.1016/S0022-2313(02)00281-8

11. J. J. Longdell, E. Fraval, M. J. Sellars, N. B. Manson, Stopped light with storage times greater than one second using electromagnetically induced transparency in a solid. *Phys. Rev. Lett.* **95**, 063601 (2005). doi:10.1103/PhysRevLett.95.063601 Medline

12. M. P. Hedges, J. J. Longdell, Y. Li, M. J. Sellars, Efficient quantum memory for light. *Nature* **465**, 1052–1056 (2010). doi:10.1038/nature09081 Medline

13. M. Afzelius, I. Usmani, A. Amari, B. Lauritzen, A. Walther, C. Simon, N. Sangouard, J. Minár, H. de Riedmatten, N. Gisin, S. Kröll, Demonstration of atomic frequency comb memory for light with spin-wave storage. *Phys. Rev. Lett.* **104**, 040503 (2010). doi:10.1103/PhysRevLett.104.040503 Medline

14. T. Zhong, J. M. Kindem, E. Miyazono, A. Faraon, Nanophotonic coherent light-matter interfaces based on rare-earth-doped crystals. *Nat. Commun.* **6**, 8206 (2015). doi:10.1038/ncomms9206 Medline

15. T. Zhong, J. M. Kindem, J. Rochman, A. Faraon, Interfacing broadband photonic qubits to on-chip cavity-protected rare-earth ensembles. *Nat. Commun.* **8**, 14107 (2017). doi:10.1038/ncomms14107 Medline

16. T. Zhong, J. Rochman, J. M. Kindem, E. Miyazono, A. Faraon, High quality factor nanophotonic resonators in bulk rare-earth doped crystals. *Opt. Express* **24**, 536–544 (2016). doi:10.1364/OE.24.000536 Medline

17. See the supplementary materials.

18. F. Marsili, V. B. Verma, J. A. Stern, S. Harrington, A. E. Lita, T. Gerrits, I. Vayshenker, B. Baek, M. D. Shaw, R. P. Mirin, S. W. Nam, Detecting single infrared photons with 93% system efficiency. *Nat. Photonics* **7**, 210–214 (2013). doi:10.1038/nphoton.2013.13

19. M. Sabooni, Q. Li, S. Kröll, L. Rippe, Efficient quantum memory using a weakly absorbing sample. *Phys. Rev. Lett.* **110**, 133604 (2013). doi:10.1103/PhysRevLett.110.133604 Medline

20. M. Afzelius, C. Simon, Impedance-matched cavity quantum memory. *Phys. Rev. A* **82**, 022310 (2010). doi:10.1103/PhysRevA.82.022310

21. S. A. Moiseev, S. N. Andrianov, F. F. Gubaidullin, Efficient multimode quantum memory based on photon echo in an optimal QED cavity. *Phys. Rev. A* **82**, 022311 (2010). doi:10.1103/PhysRevA.82.022311

22. D. L. McAuslan, J. J. Longdell, M. J. Sellars, Cavity QED using rare-earth-metal-ion dopants in monolithic resonators: What you can do with a weak oscillator. *Phys. Rev. A* **80**, 062307 (2009). doi:10.1103/PhysRevA.80.062307

23. B. Lauritzen, S. R. Hastings-Simon, H. de Riedmatten, M. Afzelius, N. Gisin, State preparation by optical pumping in erbium-doped solids using stimulated emission and spin mixing. *Phys. Rev. A* **78**, 043402 (2008). doi:10.1103/PhysRevA.78.043402

24. M. Afzelius, M. U. Staudt, H. de Riedmatten, N. Gisin, O. Guillot-Noël, P. Goldner, R. Marino, P. Porcher, E. Cavalli, M. Bettinelli, Efficient optical pumping of Zeeman spin levels in Nd^{3+}:YVO_4. *J. Lumin.* **130**, 1566–1571 (2010). doi:10.1016/j.jlumin.2009.12.026

25. N. Sinclair, E. Saglamyurek, H. Mallahzadeh, J. A. Slater, M. George, R. Ricken, M. P. Hedges, D. Oblak, C. Simon, W. Sohler, W. Tittel, Spectral multiplexing for scalable quantum photonics using an atomic frequency comb quantum memory and feed-forward control. *Phys. Rev. Lett.* **113**, 053603 (2014). doi:10.1103/PhysRevLett.113.053603 Medline

26. Z.-Q. Zhou, W.-B. Lin, M. Yang, C.-F. Li, G.-C. Guo, Realization of reliable solid-state quantum memory for photonic polarization qubit. *Phys. Rev. Lett.* **108**, 190505 (2012). doi:10.1103/PhysRevLett.108.190505 Medline

27. N. Sinclair, K. Heshami, C. Deshmukh, D. Oblak, C. Simon, W. Tittel, Proposal and proof-of-principle demonstration of non-destructive detection of photonic qubits using a

Tm:LiNbO3 waveguide. *Nat. Commun.* **7**, 13454 (2016). doi:10.1038/ncomms13454 Medline

28. R. Kolesov, K. Xia, R. Reuter, R. Stöhr, A. Zappe, J. Meijer, P. R. Hemmer, J. Wrachtrup, Optical detection of a single rare-earth ion in a crystal. *Nat. Commun.* **3**, 1029 (2012). doi:10.1038/ncomms2034 Medline

29. J. J. Longdell, M. J. Sellars, Experimental demonstration of quantum-state tomography and qubit-qubit interactions for rare-earth-metal-ion-based solid-state qubits. *Phys. Rev. A* **69**, 032307 (2004). doi:10.1103/PhysRevA.69.032307

30. G. Wolfowicz, H. Maier-Flaig, R. Marino, A. Ferrier, H. Vezin, J. J. L. Morton, P. Goldner, Coherent storage of microwave excitations in rare-earth nuclear spins. *Phys. Rev. Lett.* **114**, 170503 (2015). doi:10.1103/PhysRevLett.114.170503 Medline

31. C. O'Brien, T. Zhong, A. Faraon, C. Simon, Nondestructive photon detection using a single rare-earth ion coupled to a photonic cavity. *Phys. Rev. A* **94**, 043807 (2016). doi:10.1103/PhysRevA.94.043807

32. C. O'Brien, N. Lauk, S. Blum, G. Morigi, M. Fleischhauer, Interfacing superconducting qubits and telecom photons via a rare-earth-doped crystal. *Phys. Rev. Lett.* **113**, 063603 (2014). doi:10.1103/PhysRevLett.113.063603 Medline

33. S. R. Hastings-Simon, M. Afzelius, J. Minar, M. U. Staudt, B. Lauritzen, H. de Riedmatten, N. Gisin, A. Amari, A. Walther, S. Kröll, E. Cavalli, M. Bettinelli, Spectral hole-burning spectroscopy in Nd^{3+}:YVO_4. *Phys. Rev. B* **77**, 125111 (2008). doi:10.1103/PhysRevB.77.125111

34. E. M. Purcell, Spontaneous emission probabilities at radio frequencies. *Phys. Rev.* **69**, 681 (1946).

35. X. Ma, B. Qi, Y. Zhao, H.-K. Lo, Practical decoy state for quantum key distribution. *Phys. Rev. A* **72**, 012326 (2005). doi:10.1103/PhysRevA.72.012326